Proceedings of the
Annual Stability Conference
Structural Stability Research Council
Louisville, Kentucky, April 13-16, 2021

Beam element material models for straightened hot rolled sections and welded HSS sections

Barry T. Rosson[1]

Abstract
Inelastic material models that were previously developed by the author for standard W-Shapes were adapted for use to model the behavior and strength of rotary-straightened hot rolled sections and welded high-strength steel (HSS) sections. Using published residual stress models for these I-shape sections, limit load analyses were conducted using the material models in MASTAN2 and were compared with published experimental and finite element results. The rotary-straightened hot rolled sections were modeled as simply supported columns and beam-columns, and the material model required an adjustment to the initial yield moment conditions m_1 and the use of two residual stress ratios c_r^+ and c_r^-. The welded HSS sections were modeled as beams with a constant moment, and the material model required only a slight increase in the exponent conditions n_z and n_y. Comparisons with published results indicate that these minor modifications were sufficient to provide very good modeling agreement. The previously developed material models can be used effectively to model the limit load conditions of rotary-straightened hot rolled beam-columns and welded HSS I-section beams.

1. Introduction

Since the early 1970's, it has been known that roller-straightening hot rolled W-Shapes increases the column strength on the order of 10 to 20 percent in the *L/r* range of 40 to 100 (Alpsten 1972). This is due primarily to the fact that the rotarizing process removes, or greatly reduces, the compressive residual stresses at the flange tips for most steel columns that were manufactured during that time. Since then, modern manufacturing processes have greatly improved, with equipment and procedures that currently permit rotary-straightening of sections that weigh almost 400 lb/ft and depths up to 36 inches; thus, most sections are now rotarized (Ge and Yura 2019).

The use of high-strength steel (HSS) is gaining popularity in the construction industry because it offers superior strength, excellent weldability, acceptable ductility and high notch toughness (Le *et al*. 2020b). It has been found that the compression residual stresses in the flanges of HSS I-sections are significantly less than that of mild steel sections (Le *et al*. 2020a, Li *et al*. 2020, Unsworth *et al*. 2020). This has the potential to provide for higher load carrying capacities;

[1] Professor, Florida Atlantic University, <rosson@fau.edu>

however, only until recently have extensive laboratory and simulation studies been conducted on the flexural strength of HSS members (Sun *et al*. 2019, Le *et al*. 2020b, Wang *et al*. 2020).

For compact W-Shapes with an ECCS residual stress distribution pattern (1984), the stiffness reduction that results from yielding of the cross-section due to uniaxial bending and axial compression was studied in detail by Rosson (2016). Three-dimensional *m-p-*τ surface plots were used to discuss the stress states around the perimeter of the surfaces and to develop an inelastic material model in MASTAN2 that was accurate and easy to use when determining the limit load capacity of beam-columns and frames (Rosson 2018, Rosson and Ziemian 2019). Further development of the inelastic material model included the enhancement of normalized tangent modulus expressions in MASTAN2 for combined major axis and minor axis beam bending conditions using a 14-DOF beam element to determine the lateral-torsional buckling capacity of rolled I-section beams (Rosson and Fadden 2020). The objective of this study is to demonstrate that these previously developed inelastic material models can be adapted for use in modeling the behavior of rotary-straightened hot rolled beam-columns and welded HSS I-section beams.

2. Stiffness Reduction Models

2.1 Inelastic material model for beam-columns with major axis bending or minor axis bending

As previously demonstrated in Rosson (2018), the extent of τ = 1 is determined when the moment and axial load conditions cause all three compression stresses to sum to σ_y. The maximum moment at which τ = 1 is maintained for minor axis bending is given as

$$m_1 = \frac{S_y}{Z_y}(1 - c_r - p) \tag{1}$$

where m = normalized moment (M/M_p), S_y = minor axis elastic section modulus, Z_y = minor axis plastic section modulus, c_r = residual stress ratio (σ_r/σ_y), and p = normalized axial load (P/P_y). The sign on P_y matches that of P such that p is always positive. Since this equation is based only on the accumulation of compression stress at the end of each flange, the actual shape of the residual pattern does not affect the equation provided the maximum residual compression stress σ_r occurs at the end of the flanges. The maximum moment at which τ = 1 is maintained for major axis bending is determined in a similar manner to Eq. 1 and is found to be

$$m_1 = \frac{S_z}{Z_z}(1 - c_r - p) \tag{2}$$

where S_z = major axis elastic section modulus and Z_z = major axis plastic section modulus. Since this equation is based only on the accumulation of compression stress in the flange, the actual shape of the residual pattern does not affect Eq. 2. Two equations are needed to determine the moment and axial load conditions when τ = 0 for the minor axis bending and major axis bending conditions. For the minor axis bending condition, one equation is needed when the plastic neutral axis is inside the web thickness, and the other is needed when it is outside the web thickness.

$$when\ \ p < \frac{2\lambda_o + \lambda}{2 + \lambda} \qquad m_0 = 1 - \frac{p^2(2 + \lambda)^2}{(2 + \lambda\lambda_o)(2 + \lambda_1)} \tag{3}$$

$$when\ \ p \geq \frac{2\lambda_o + \lambda}{2 + \lambda} \qquad m_0 = \frac{4 - [p(2+\lambda) - \lambda]^2}{2(2 + \lambda\lambda_o)} \tag{4}$$

where $\lambda = A_w/A_f$, $\lambda_o = t_w/b_f$ and $\lambda_1 = d_w/t_f$. For the major axis bending condition, one equation is needed when the plastic neutral axis is outside the flange thickness, and the other is needed when it is inside the flange thickness.

$$when\ \ p < \frac{\lambda}{2 + \lambda} \qquad m_0 = 1 - \frac{p^2(2+\lambda)^2}{4\lambda_o + \lambda(4+\lambda)} \tag{5}$$

$$when\ \ p \geq \frac{\lambda}{2 + \lambda} \qquad m_0 = \frac{(2+\lambda_1)^2 - [p(2+\lambda) - \lambda + \lambda_1]^2}{4 + \lambda_1(4+\lambda)} \tag{6}$$

Eqs. 3 through 6 do not depend upon the shape of the residual stress pattern.

Referring to Fig. 1, there is no stiffness reduction (τ = 1) for moment and axial load conditions inside the triangular region defined by m_1, and when the moment and axial load conditions are between m_1 and m_0, the stiffness reduction τ can be easily determined using Eqs. 7 and 8. Eqs. 1, 3 and 4 are used for minor axis bending, and Eqs. 2, 5 and 6 for major axis bending.

$$when\ \ p < 1 - c_r \qquad \tau = 1 - \left(\frac{m - m_1}{m_0 - m_1}\right)^n \tag{7}$$

$$when\ \ p \geq 1 - c_r \qquad \tau = \left(\frac{1-p}{c_r}\right)\left(1 - \frac{m}{m_0}\right)^n \tag{8}$$

The material model allows for the independent input of the n value and the residual stress ratio c_r.

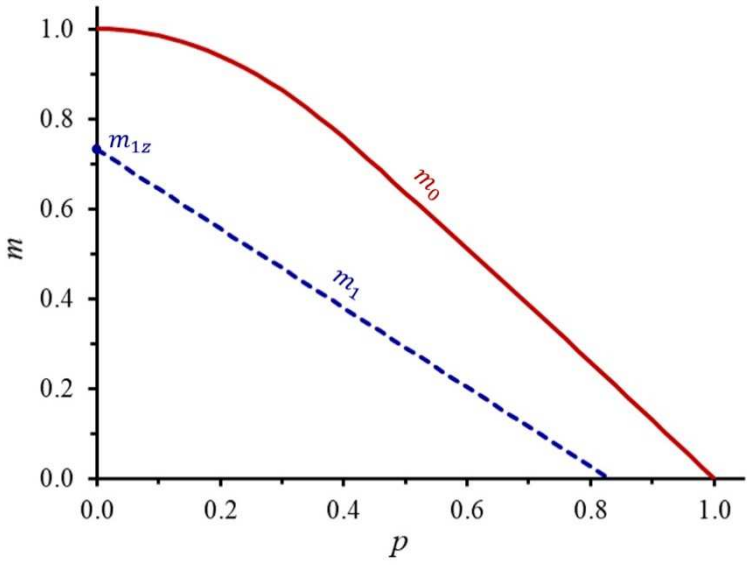

Figure 1: m_1 and m_0 perimeter conditions for beam-column with major axis bending

2.2 Inelastic material model for beams with both major axis and minor axis bending

The stiffness reduction model that accounts for partial yielding of the beam's cross-section due to biaxial bending moments was developed by Rosson and Fadden (2020). The model in Fig. 2 is not dependent upon a particular residual stress pattern other that the maximum compression residual stress in the flanges must occur at the ends. The triangular plateau at the top of the model represents the moment conditions for which yielding does not occur (τ = 1). The dashed red curve represents the stiffness reduction due to moments beyond the yield plateau and is assumed to vary as an exponential function between 1 and 0. The blue curve at the bottom represents the biaxial moment conditions at which τ = 0 and is assumed to vary as a second-order polynomial defined by the three coordinates $(1,0,0)$, $(m_z^*, m_y^*, 0)$ and $(0,1,0)$. The m_z^* and m_y^* values are a function of I-section's cross-section dimensions (Rosson and Fadden 2020).

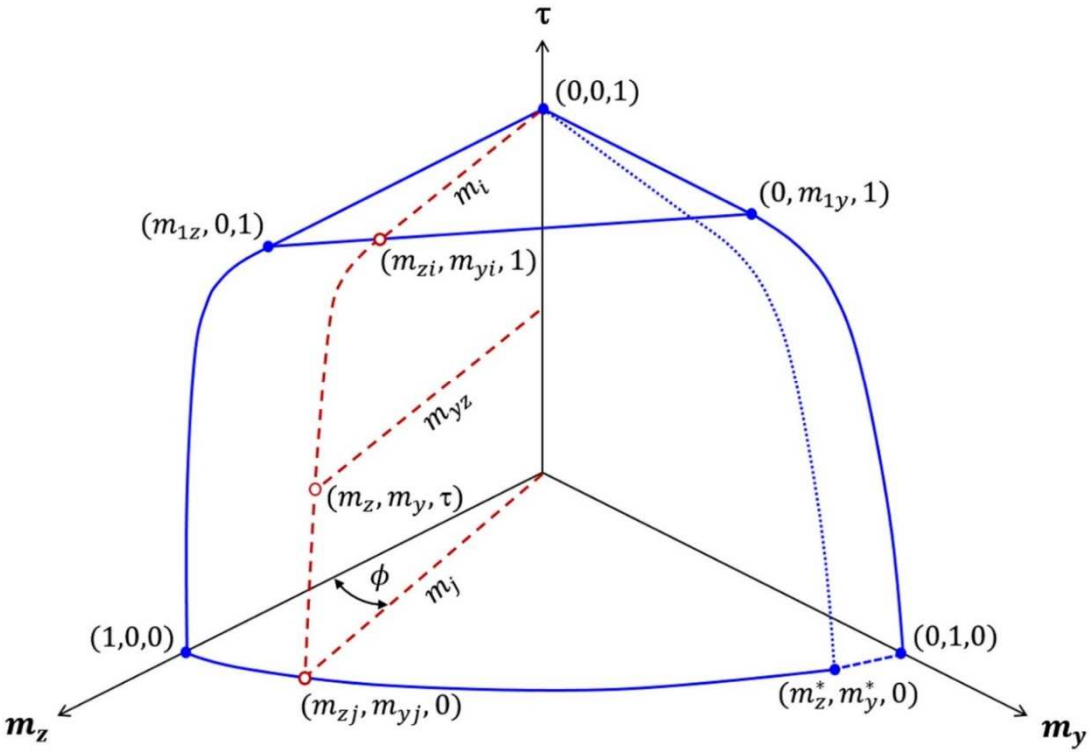

Figure 2: Stiffness reduction model with variable definitions for major axis and minor axis bending

The major axis moment M_z and minor axis moment M_y are normalized using the respective plastic moment capacities as $m_z = M_z/M_{pz}$ and $m_y = M_y/M_{py}$. For a given I-section, the maximum moment for which τ = 1 is maintained for uniaxial major axis bending is

$$m_{1z} = \frac{S_z}{Z_z}(1 - c_r) \tag{9}$$

A similar expression for uniaxial minor axis bending is

$$m_{1y} = \frac{S_y}{Z_y}(1 - c_r) \tag{10}$$

The m_{yz} scalar magnitude in Fig. 2 is given as

$$m_{yz} = \sqrt{m_z^2 + m_y^2} \tag{11}$$

For a given m_z and m_y biaxial moment condition, the stiffness reduction can be determined using Eqs. 12 and 13. Refer to the paper by Rosson and Fadden (2020) for the development of all the remaining variables presented in Fig. 2.

$$when \;\; m_{yz} \leq m_i \qquad\qquad \tau = 1 \tag{12}$$

$$when \;\; m_i < m_{yz} \leq m_j \qquad \tau = 1 - \left(\frac{m_{yz} - m_i}{m_j - m_i}\right)^{n_b} \tag{13}$$

where the exponent n_b is a function of the m_y/m_z ratio and the n_z and n_y input values.

$$n_b = (n_z - n_y)e^{\left(\frac{-\pi}{5}\frac{m_y}{m_z}\right)} + n_y \tag{14}$$

2.3 Residual stresses

The residual stresses in a rotary-straightened W12x65 were measured by Ge and Yura (2019) using the sectioning method. Based on their results, they proposed the idealized residual stress pattern given in Fig. 3(a). The residual compression stresses in the flanges σ_{rfc} are no longer at the ends and are significantly reduced due to the rotary-straightening process. The maximum residual tension stresses σ_{rft} are now at the flange ends and will affect the initial yield conditions under low compression load conditions. The reduced magnitude of σ_{rfc} can be easily accounted for with the appropriate value for c_r^-, but the m_1 equation now must be based on the new location of σ_{rfc} at the quarter point of the flanges. Using σ_{rfc} to calculate c_r^- in Eq. 1, the maximum moment to avoid initial compression yield with minor axis bending is given as

$$when \;\; 1 - 2c_r^- + c_r^+ < \; p \leq 1 - c_r^- \qquad m_1^- = \frac{2S_y}{Z_y}(1 - c_r^- - p) \tag{15}$$

Using σ_{rft} to calculate c_r^+, the maximum moment to avoid initial compression yield under moderate compression load conditions with minor axis bending is given as

$$when \;\; c_r^+ < p \leq 1 - 2c_r^- + c_r^+ \qquad m_1^{\pm} = \frac{S_y}{Z_y}(1 + c_r^+ - p) \tag{16}$$

The maximum moment to avoid initial tension yield under low compression load conditions with minor axis bending is given as

$$when \;\; p \leq c_r^+ \qquad\qquad m_1^+ = \frac{S_y}{Z_y}(1 - c_r^+ + p) \tag{17}$$

Using σ_{rfc} to calculate c_r^- in Eq. 2, the maximum moment to avoid initial compression yield in the flange with major axis bending is given as

$$when\ \frac{c_r^+ - c_r^-}{2} < p \le 1 - c_r^- \qquad m_1^- = \frac{S_z}{Z_z}(1 - c_r^- - p) \tag{18}$$

Using σ_{rft} to calculate c_r^+, the maximum moment to avoid initial tension yield in the flange under low compression load conditions for major axis bending is given as

$$when\ p \le \frac{c_r^+ - c_r^-}{2} \qquad m_1^+ = \frac{S_z}{Z_z}(1 - c_r^+ + p) \tag{19}$$

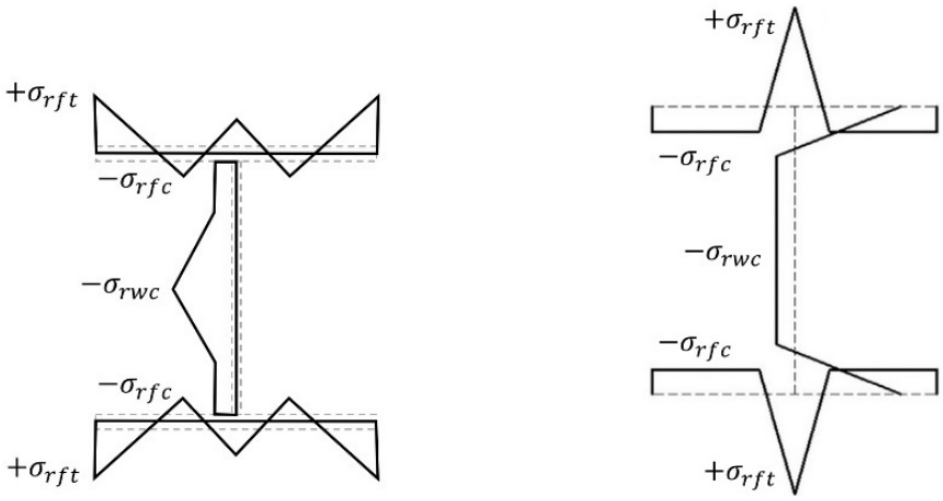

(a) Rotary-straightened hot rolled steel section (b) Welded high-strength steel section

Figure 3: Idealized residual stress models

The residual stress model for welded HSS sections that is given in Fig. 3(b) is based on residual stress measurements by Le *et al*. (2020a). The compression residual stresses are approximately uniform across much of the flange length. Its magnitude is independent of the base metal strength and is solely a function of the flange dimensions (Le *et al*. 2020b).

$$\sigma_{rfc} = 140 - 16t_f + 0.4t_f^2 + 820t_f/b_f \tag{20}$$

Since the σ_{rfc} stresses occur at the flange ends, the previously developed inelastic material model for W-Shape beams can be used with modification only to the n_z and n_y input values.

3. Material Model Validation Study

The column and beam-column test conditions for the rotarized W12x65 in Ge and Yura (2019) were used to study the effectiveness of the inelastic material model given by Eqs. 3 through 8 and Eqs. 15 through 19. The W-shape is assumed to be fully-compact and its out-of-plane behavior fully restrained. The beam test conditions for four welded HSS I-sections in Le *et a*l. (2020b) were used to investigate the inelastic material model given by Eqs. 9 through 14 and Eq. 20. The four beams that were selected for the study failed due to lateral-torsional buckling.

3.1 Rotary-straightened W12x65 modeling results

Based on the values σ_{rfc} = 5 ksi, σ_{rft} = 10 ksi and σ_y = 50 ksi given by Ge and Yura (2019), the residual stress ratios used in the study were c_r^- = 0.1 and c_r^+ = 0.2. The initial geometric imperfections were directly modeled using the first eigen-mode normalized to L/1000 at mid-height. The column analyses in MASTAN2 were conducted using a second-order inelastic analysis with E = 29,000 ksi, n_y = 1.2 for minor axis bending and n_z = 1.5 for major axis bending. For consistency with past research, both exponent values n_z and n_y are the same as those used for the W-Shapes in the study by Rosson and Fadden (2020). The inelastic material model for the rotarized W12x65 is given in Fig. 4 for minor axis bending. The effects of Eqs. 15 through 17 on the yield plateau region are evident with the dashed blue lines.

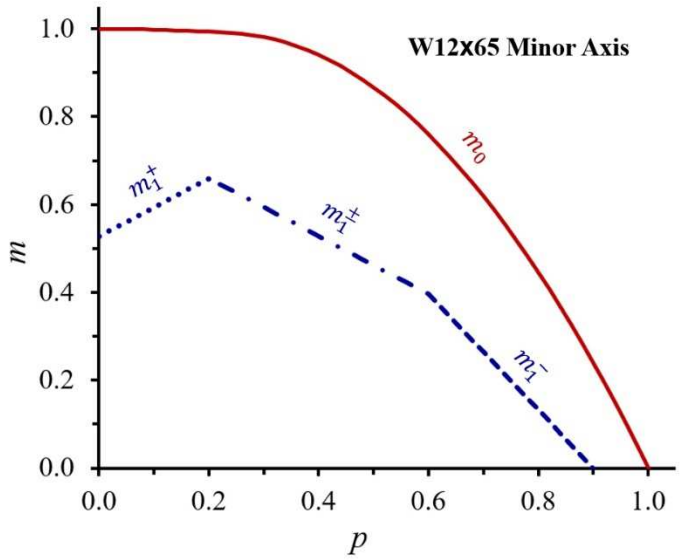

Figure 4: m_1 and m_0 perimeter conditions for rotarized W12x65 beam-column with minor axis bending

The inelastic material model for major axis bending is given in Fig. 5. Comparing it with Fig. 1, the effects of Eqs. 18 and 19 on the τ = 1 region are evident with the dotted and dashed blue lines.

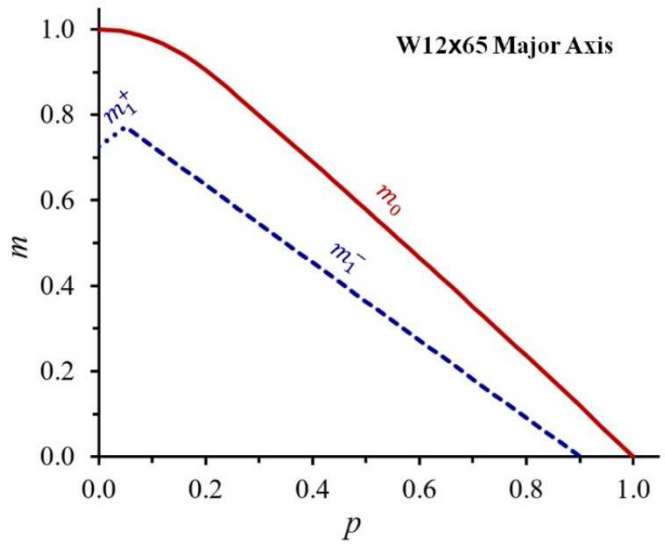

Figure 5: m_1 and m_0 perimeter conditions for rotarized W12x65 beam-column with major axis bending

Column limit load analyses for minor axis bending and major axis bending were conducted on pinned-pinned columns using 10 beam elements in MASTAN2. They were compared with the ABAQUS column strength results by Ge and Yura (2019) and the AISC (E3-2) and (E3-3) equations (2016). The results in Figs. 6 and 7 indicate very close agreement between the inelastic material models used in MASTAN2 and the more detailed ABAQUS finite element models. Due to the large $\tau = 1$ plateau regions in Figs. 4 and 5, the limit load results are considerably higher than the AISC solutions for the shorter unbraced lengths ($\lambda < 1$).

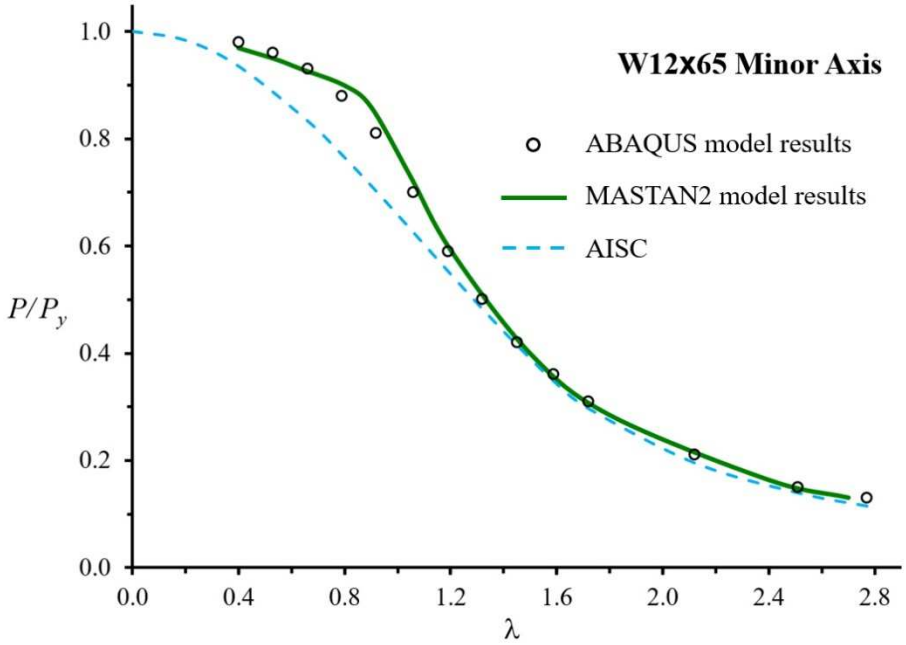

Figure 6: Comparison of W12x65 minor axis bending column results

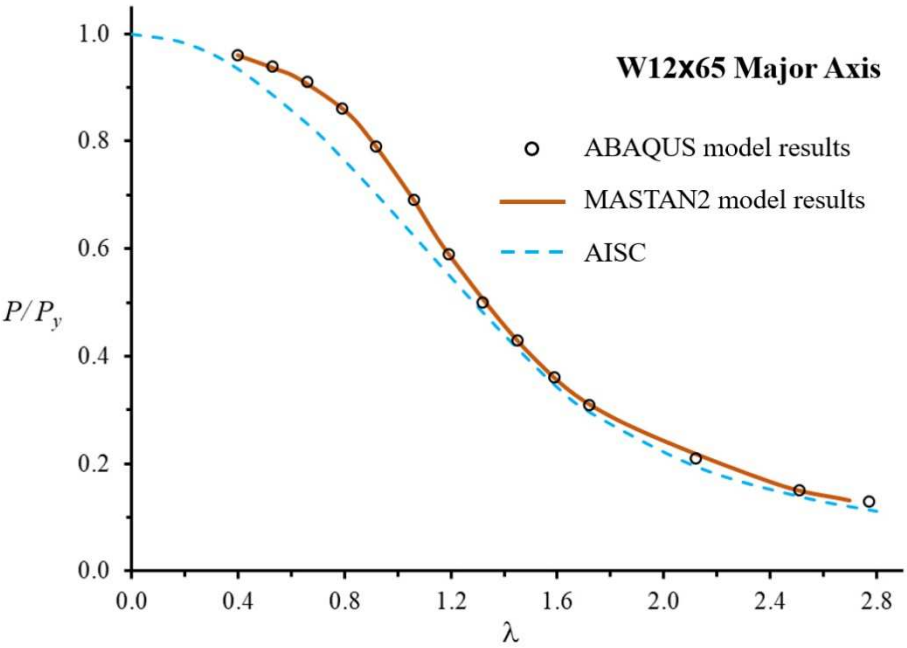

Figure 7: Comparison of W12x65 major axis bending column results

The beam-column in Fig. 8 was studied by Ge and Yura (2019) using the rotary-straightened W12x65 with L/r = 80 and axial load conditions of P/P_y = 0.4 and 0.5. The MASTAN2 model used 20 beam elements with major axis bending and the same inelastic material model constants c_r^- = 0.1, c_r^+ = 0.2 and n_z = 1.5 as before. The specified axial load P was first incrementally applied to the beam-column model with an L/1000 initial geometric imperfection, then the horizontal load H was incrementally applied until the limit load was reached.

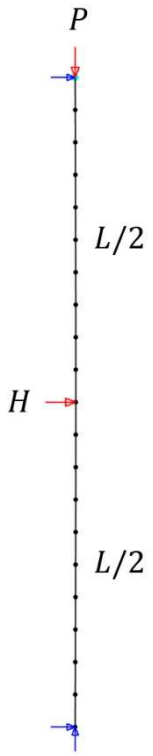

Figure 8: MASTAN2 model of laterally loaded beam-column used by Ge and Yura (2019)

The displacements in Fig. 9 are only the horizontal displacements occurring at mid-span during the application of the lateral load. Comparing the MASTAN2 and ABAQUS model results, the mid-span displacement Δ and applied lateral load H are approximately the same at the limit load for the P/P_y = 0.5 condition, but they vary by approximately 8% when the limit load is reached for the P/P_y = 0.4 condition. In general, the MASTAN2 model maintained higher flexural stiffness conditions after the application of the vertical load P, and the inelastic material model reduced the stiffness in a similar manner to the ABAQUS model as the lateral load H was applied. Contrasting the very close results in Fig. 7 with those in Fig. 9 indicates that the material model constants are perhaps more sensitive for the beam-column models compared with the simpler pinned-pinned column models. Additional research is needed to determine the extent to which the inelastic material model constants c_r and n affect the beam-column results and under what conditions they have the greatest influence.

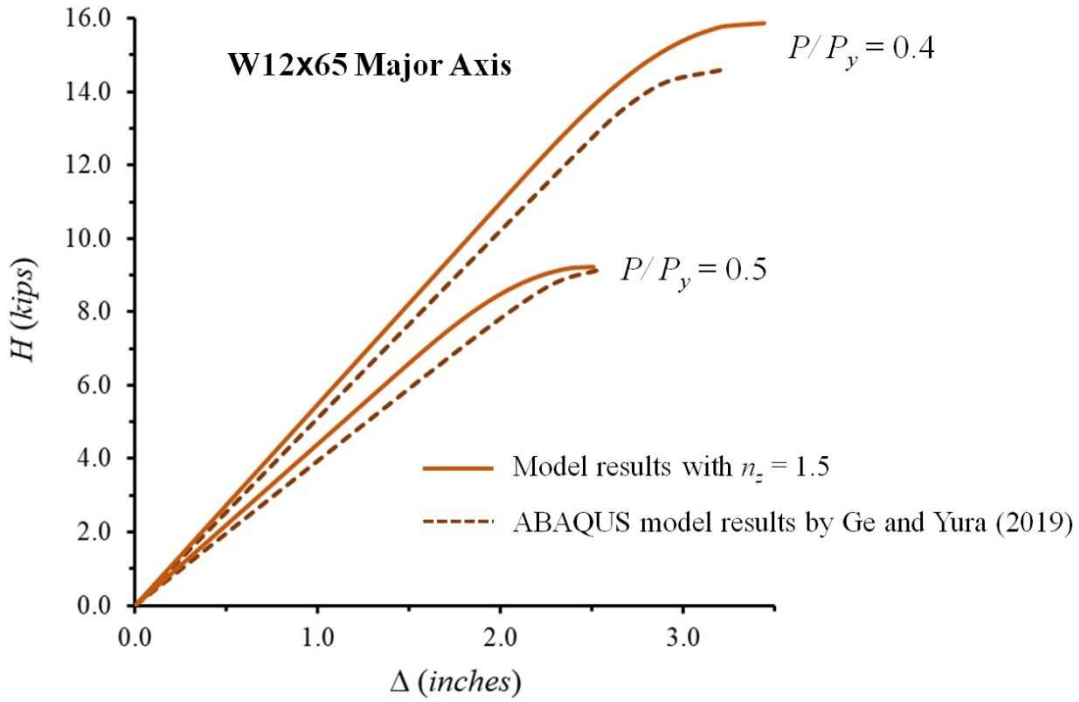

Figure 9: Model results compared with simulation results by Ge and Yura (2019)

3.2 Welded HSS I-section modeling results

The beam in Fig. 10 was studied by T. Le *et al*. (2020b) using welded HSS I-sections with yield strengths of 690 MPa (100 ksi) and 890 MPa (130 ksi). They conducted several different laboratory tests, but the four selected for this study included those that failed due to flexural-torsional buckling under uniform bending moment conditions. The specimen cross-section dimensions and material properties of the four beams are given in Table 1. The c_r values were determined using the listed σ_y values and Eq. 20 for the compression residual stress in the flange σ_{rfc} based on the listed b_f and t_f values. The test specimens had out-of-plumb imperfections between 1.75 mm and 2.5 mm. The loads in the laboratory were applied through loading boxes which restrained the beam against lateral deflection and twist, but which allowed it to rotate freely about the major and minor axes and to warp and move in-plane.

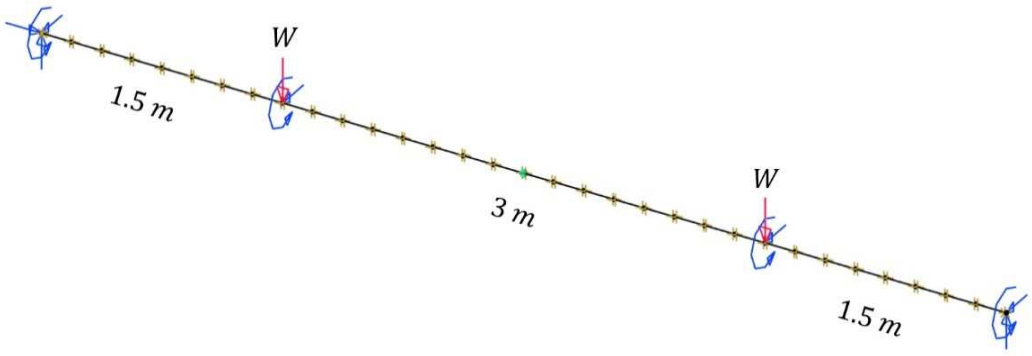

Figure 10: MASTAN2 model of 4-point loading condition used by T. Le *et al*. (2020b)

Table 1: Specimen cross-section dimensions and material properties

Specimen	d (mm)	b_f [1] (mm)	t_f (mm)	t_w (mm)	E (GPa)	σ_y (MPa)	c_r
I-690-3	354.3	76.15	11.77	7.70	195	800	0.17
I-890-3	354.0	76.13	11.80	7.95	198	1000	0.13
I-890-4	353.8	56.18	11.80	7.95	198	1000	0.18
I-890-5	254.5	56.13	11.80	7.95	198	1000	0.18

1. The b_f dimension defined by T. Le *et al*. (2020b) is measured from the web to the end of the flange

The MASTAN2 models used an initial geometric imperfection of 3 mm at mid-span and a total of 32 beam elements with 16 elements between the two loads. The material model used n_z = 2 for major axis bending and n_y = 1.5 for minor axis bending. The two W loads in Fig. 10 were incrementally applied using a second-order inelastic analysis up to the limit load condition.

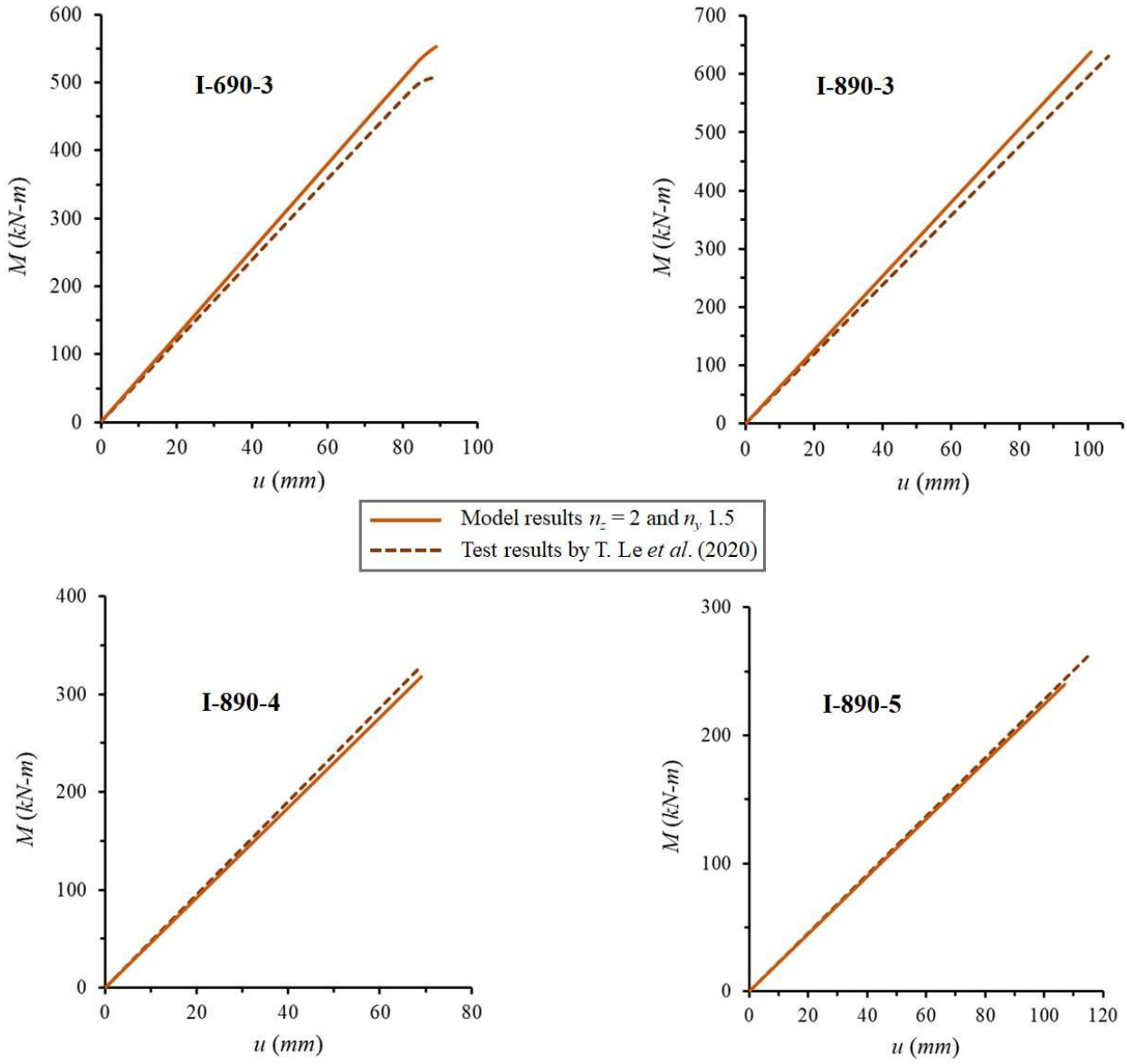

Figure 11: MASTAN2 model results compared with laboratory test results by T. Le *et al*. (2020b)

The MASTAN2 and laboratory test results for the four HSS I-sections are given in Fig. 11. In general, the models reveal similar limit load conditions of maximum mid-span moment and vertical deflection. Since the material model constants n_z and n_y were the same for all four beam conditions, it appears that there may not be a need to update these values based on the cross-section dimensions and material properties. The modeled results are sensitive to the c_r value, but it appears sufficient to simply calculate this value using the residual stress relationship in Eq. 20 and the tensile stress at first yield for the σ_y value; however, more research is needed to verify the findings regarding the material constants.

4. Conclusions

The inelastic material models that were previously developed by the author were used to model rotary-straightened W-Shapes and welded HSS I-sections. Because of their unique residual stress patterns, modifications were necessary to use the existing material models. To model the rotarized W-Shapes, additional equations for the initial yield moment m_1 were required and separate c_r values were needed based on the compression residual stress σ_{rfc} and tension residual stress σ_{rft}. To model the welded HSS I-section, it was only necessary to use the σ_{rfc} based on the flange cross-section properties and slightly higher values for n_z and n_y. Validation studies compared the modeled results with those found in the literature, and it was determined that they provided similar limit load results when using the existing inelastic material models with these minor modifications.

References

ABAQUS Version 6.12-1. Dassault Systèmes, Waltham, MA.

Alpsten, G. (1972). "Residual stresses, yield stress and column strength of hot-rolled and roller-straightened steel shapes." *Proceedings of the First International Colloquium on Stability*, Paris, France.

AISC. (2016). "Specification for structural steel buildings." *ANSI/AISC 360-16*, Chicago, IL.

ECCS. (1984). "Ultimate limit state calculation of sway frames with rigid joints." *TC 8 of European Convention for Constructional Steelwork*, No. 33.

Ge X., Yura J.A. (2019). "The strength of rotary-straightened steel columns." *Proceedings of the 2019 SSRC Annual Stability Conference*, St. Louis, Missouri.

Le T., Paradowska A., Bradford M.A., Liu X., Valipour H.R. (2020a). "Residual stresses in welded high-strength steel I-beams." *Journal of Constructional Steel Research*, 167 105849.

Le T., Bradford M.A., Liu X., Valipour H.R. (2020b). "Buckling of welded high-strength steel I-beams." *Journal of Constructional Steel Research*, 168 105938.

Li D., Paradowska A., Uy B., Wang J., Khan M. (2020). "Residual stresses of box and I-shaped columns fabricated from S960 ultra-high-strength steel." *Journal of Constructional Steel Research*, 166 105904.

MASTAN2 Version 3.5. Ziemian R.D., McGuire W.

Rosson B.T. (2016). "Elasto-plastic stress states and reduced flexural stiffness of steel beam-columns." *Proceedings of the 2016 SSRC Annual Stability Conference*, Orlando, Florida.

Rosson B.T. (2018). "Modeling the influence of residual stress on the ultimate load conditions of steel frames." *Proceedings of the 2018 SSRC Annual Stability Conference*, Baltimore, Maryland.

Rosson B.T., Ziemian R.D. (2019). "Validation study of a new inelastic material model for steel W-Shapes." *Proceedings of the 2019 SSRC Annual Stability Conference*, St. Louis, Missouri.

Rosson B.T., Fadden, M.F. (2020). "Modeling the nominal flexural strength of w-shape beams using a new inelastic model." *Proceedings of the 2020 SSRC Annual Stability Conference*, Atlanta, Georgia.

Sun Y., He A., Liang L., Zhao O. (2019). "In-plane bending behaviour and capacities of S690 high strength steel welded I-section Beams." *Journal of Constructional Steel Research*, 162 105741.

Unsworth D., Driver R.G., Li J. (2020). "Measurement and prediction of residual stresses in welded girders." *Journal of Constructional Steel Research*, 169 106007.

Wang Y., Bradford M.A., Liu X. (2020). "Strength design of welded high-strength steel beams considering coupled local and global buckling." *Thin-Walled Structures*, 149 106391.